

Distinct dynamics of self-propelled bowl-shaped micromotors caused by shape effect: Concave vs convex

Cite as: Phys. Fluids **33**, 122004 (2021); <https://doi.org/10.1063/5.0076060>

Submitted: 20 October 2021 • Accepted: 20 November 2021 • Published Online: 07 December 2021

Duo Wang, Dongshi Guan,  Jinghong Su, et al.



View Online



Export Citation



CrossMark

ARTICLES YOU MAY BE INTERESTED IN

[Diffusiophoresis of a highly charged dielectric fluid droplet](#)

Physics of Fluids **33**, 122005 (2021); <https://doi.org/10.1063/5.0069778>

[Hydrodynamic analysis of fish schools arranged in the vertical plane](#)

Physics of Fluids **33**, 121905 (2021); <https://doi.org/10.1063/5.0073728>

[Evaporation kinetics of sessile droplets morphed by substrate curvature](#)

Physics of Fluids **33**, 122010 (2021); <https://doi.org/10.1063/5.0074882>

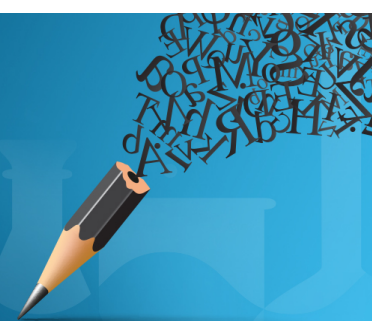


Author Services

English Language Editing

High-quality assistance from subject specialists

LEARN MORE



Distinct dynamics of self-propelled bowl-shaped micromotors caused by shape effect: Concave vs convex

Cite as: Phys. Fluids **33**, 122004 (2021); doi: 10.1063/5.0076060

Submitted: 20 October 2021 · Accepted: 20 November 2021 ·

Published Online: 7 December 2021






View Online



Export Citation



CrossMark

Duo Wang,^{1,2,3} Dongshi Guan,^{2,3} Jinghong Su,^{1,2,3}  Xu Zheng,^{2,a)}  and Guoqing Hu^{1,a)} 

AFFILIATIONS

¹Department of Engineering Mechanics, State Key Laboratory of Fluid Power and Mechatronic Systems, Zhejiang University, Hangzhou 310027, China

²The State Key Laboratory of Nonlinear Mechanics (LNM), Institute of Mechanics, Chinese Academy of Sciences, Beijing 100190, China

³School of Engineering Science, University of Chinese Academy of Sciences, Beijing 100049, China

^{a)}Authors to whom correspondence should be addressed: zhengxu@lnm.imech.ac.cn and ghu@zju.edu.cn

ABSTRACT

Although artificial micromotors with unconventional shapes are emerging as a powerful tool in various applications, little research has been undertaken to clarify their propulsion mechanism, especially how the shape effect alters the bubble dynamics and hydrodynamic flows. In this study, we fabricated two types of bowl-shaped micromotors to investigate the distinct dynamics due to the shape effect of concave and convex surfaces, by coating a platinum (Pt) layer on either the concave surface or the convex surface of the micromotor. In the single-bubble propulsion mode at low fuel concentration, the concave-surface-Pt-coated micromotor moved unexpectedly slower than the convex-surface-Pt-coated micromotor, and the bubble growth on the concave surface was also much slower than that on the convex surface. It was elucidated that the confinement effect of the concave surface hindered fuel replenishment and thus the catalytic reaction. We further introduced the Kelvin impulse to explain why the concave shape eventually weakened the propulsion from hydrodynamic jet flows caused by bubble collapse. In the multi-bubble propulsion mode at high fuel concentration, the interaction among bubbles rendered a “more is less” phenomenon—increasing in the fuel concentration did not enhance the maximum instantaneous propulsion speed. These findings inspire the development of new manipulation strategies utilizing the unconventional shape effect in micromotors.

Published under an exclusive license by AIP Publishing. <https://doi.org/10.1063/5.0076060>

I. INTRODUCTION

Artificial self-propelled micromotors^{1,2} can navigate autonomously in different fluidic environments by harvesting chemical,^{3–6} electromagnetic,^{7,8} or optical^{9,10} energies into kinetic energy. They have been tweaked for different applications, such as drug delivery,^{11–13} environmental decontamination,^{14–17} noninvasive surgery,^{12,18} and biosensing.^{19–21} Among various mechanisms to steer micromotors,^{22–24} the propulsion by impulse from bubble growth and hydrodynamic jet flow from bubble collapse is one of the most attractive ways due to its high efficiency and fast locomotion speed.^{3,25–28} For instance, compared with traditional phoretic micromotors, bubble-propelled micromotors usually result in much higher speed,^{4,27,28} and their efficiency can be further improved by employing the impact of strong jet flows. Compared with other micromotors driven by external fields, the bubble-propelled micromotor is self-motile without any additional energy

input.^{2,28} Conventional bubble-propelled micromotors include tubular micromotors^{29–31} with a catalytic surface fabricated in their intracavity and spherical Janus micromotors^{32,33} with hemispherical catalytic layer covering their outer surface. The emergence of these fascinating bubble phenomena introduces rich physics of bubble dynamics and fluid flow, which has attracted broad research interest in the field of fluid dynamics.^{26,34–36}

Given that micromotors with small length scales operate at a low-speed condition in most cases, it is commonly accepted that the related flow is a low-Reynolds number (Re) Stokes flow in which the shape effect of the micromotor does not play a significant role.^{37–40} However, strong jets from bubble collapse on the micromotor surface often push the Re number so high that the above assumption becomes invalid.^{25,26,32,33} As a consequence, inertia should be taken into account in characterizing the motion of bubble-propelled

micromotors. The bubble's impact has been recognized as a fundamental issue, including bubble dynamics near an interface,^{38,41} bubble–particle interaction,^{42,43} and bubble induced flow.²⁵ In addition, due to the high ratio of surface to volume in micromotors, the shape effect of bubble-propelled micromotors is naturally deemed as a crucial factor,^{22,44–46} not only for promoting propulsion efficiency but also for strengthening their function in practical applications. Compared to the widespread symmetric spherical or tubular micromotors, micromotors with unconventional shapes possess unique benefits. For instance, microshell and microcap motors showed advantages of taking extra cargos and decorating functionalized interface using their concave side for drug delivery or biosensing.^{19,40} Different from the uncontrollable bidirectional behavior of symmetric tubular motors, conical micromotors resulted in unidirectional motion for better manipulation.^{45,47} In particular, recent studies demonstrated the possibility of manipulating the propulsion of micromotors by designing specific shapes,^{48–52} which has received considerable attention from both fundamental and applied research. Meanwhile, predicting the motion of bubble-driven micromotors becomes a challenging task because asymmetric shapes with different curvatures will dramatically influence the bubble dynamics, which could even be counter-intuitive.

In this work, we employed bowl-shaped micromotors fabricated by the microfluidic technique to address the contributions of shape asymmetry and curvature effect on bubble propulsion. By coating a platinum (Pt) layer on either the inner concave surface or the outer convex surface, we obtained two different micromotors—the concave-surface-Pt-coated micromotor and the convex-surface-Pt-coated micromotor (hereafter referred to as concave micromotor and convex micromotor). It was found that as the Re number became larger than unity during strong propulsion, the shape effect caused distinct bubble dynamics and hydrodynamic mechanisms for these two micromotors, resulting in different propulsion characteristics. More surprisingly, when the single bubble propulsion model turned into a multi-bubble model, we discovered an intriguing more is less phenomenon, indicating that high fuel concentration does not necessarily enhance the maximum propulsion speed of micromotors. This study clarifies the mechanisms underlying bubble-driven micromotor propulsion and provides a feasible manipulation strategy based on the shape effect.

II. EXPERIMENTAL METHODS

A. Fabrication of bowl-shaped micromotors

A flow-focusing capillary microfluidic device was used to fabricate bowl-shaped microparticles. The microfluidic device was made by assembling two coaxially aligned circular capillaries with different tip sizes into a square tube [Fig. 1(a)]. The detailed fabrication process can be found in our previous work⁵³ and the [supplementary material](#). The immiscible solutions shown in Fig. 1(a) are silicone oil [Sigma-Aldrich, density 0.93 g/cm^3 , kinematic viscosity 10 cSt , the yellow phase in Fig. 1(a)]; photocurable solution containing 1,6-hexanediol diacrylate [HDDA, density 1.02 g/cm^3 , dynamic viscosity $6.27 \text{ mPa}\cdot\text{s}$, the blue phase in Fig. 1(a)]; and de-ionized aqueous solution [the green phase in Fig. 1(a)] containing 1.0 wt. % sodium dodecyl sulfate (SDS) and 60% glycerol, respectively. The corresponding flow rates of these three phases are $Q_1 = 0.4 \text{ ml/h}$, $Q_2 = 0.6 \text{ ml/h}$, and $Q_3 = 6 \text{ ml/h}$, respectively. Janus microparticles with diameter ranging from $125.6 \mu\text{m}$ to $136.5 \mu\text{m}$ were generated after *in situ* curing by a LED

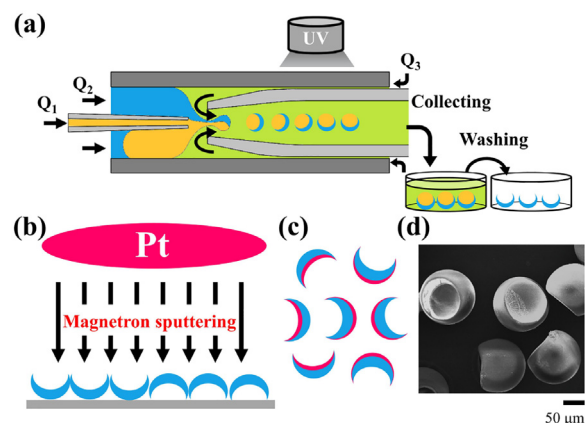


FIG. 1. Schematic of droplet-based synthesis for bowl-shaped micromotors. (a) Generation of bowl-shaped microparticles from the Janus microdroplets in a capillary microfluidic device. The inner (yellow), middle (blue), and outer (green) phases here are silicone oil, photocurable solution, and aqueous solution containing SDS and glycerol, respectively. Q_1 , Q_2 , and Q_3 are the volumetric flow rates of the inner, middle, and outer phases, respectively. (b) Fabrication of the two types of bowl-shaped HDDA micromotors (blue) by magnetron sputtering with platinum (Pt) coating. (c) Sketch of the bowl-shaped micromotors with a Pt-coating (magenta) on either concave or convex surfaces. (d) SEM image of the bowl-shaped micromotors.

UV curing system (ThorLabs, Inc., USA) in the collecting capillary. Using ethanol to remove the non-curable reagents, the bowl-shaped HDDA microparticles (blue in Fig. 1) were obtained. Finally, a magnetron sputtering coating process [Fig. 1(b)] was used to evaporate a 20 nm thick Pt layer [magenta in Figs. 1(b) and 1(c)] on the top surface of the bowl-shaped HDDA microparticles. As the bowl-shaped particles have two opposite orientations on the substrate, we obtained two different types of HDDA–Pt Janus micromotors by sputtering coating—one with Pt coating on the inner concave surface and another with Pt coating on the outer convex surface [Fig. 1(c)].

B. Observation of the self-propulsion of micromotors

The self-propulsion of micromotors originates from the catalytic decomposition of hydrogen peroxide (H_2O_2) on the Pt surface. The volumetric concentration of the H_2O_2 solution here was set to 5% for the single-bubble propulsion mode and 10% for the multi-bubble propulsion mode. The density and viscosity of the H_2O_2 solution were similar to those of water, as the H_2O_2 concentration was not high. The experiments were performed in a 30 mm plastic Petri dish, in which the concave/convex micromotors were mixed with the H_2O_2 solution. The temperature during experiments was $22\text{--}23^\circ\text{C}$. In order to avoid interaction between micromotors, we limited the number of micromotors added to the Petri dish. The motions of the micromotors were observed with an inverted microscope (Nikon Eclipse Ti-U, with $4\times$ or $10\times$ objectives). A high-speed video camera (Phantom v7.3) was used to record the motion of micromotors and the growth of bubbles. The videos were recorded at 1000 fps. A software video spot tracker (V07.02) was used to track the trajectories of the micromotors from the videos. We then used an in-house MATLAB program to calculate the displacement and mean squared displacement (MSD)

of individual micromotors. In addition, the size variations of the bubbles were measured by the software ImageJ. More measurement details can be found in the [supplementary material](#).

C. Numerical simulation

A finite element method based on COMSOL Multiphysics (version 5.5) was used to simulate the concentration of H_2O_2 and O_2 when a bubble had been generated on the concave and the convex surfaces. The self-propulsion of the micromotors involved surface catalytic reaction, mass transfer, bubble dynamics, etc. To focus on how the shape effect impacted the mass transfer and concentration field, which also influenced the catalytic reaction, we simulated the flow field and the concentration field. The simulation results provided the concentration variations of H_2O_2 and O_2 to characterize the mass transfer and catalytic reaction near a concave or a convex surface. The diameters of the bowl-shaped micromotor and the bubble were set as 130 and 140 μm , respectively. The positions of the bowl-shaped micromotor and the bubble were fixed in the simulation. The diffusion coefficients of H_2O_2 and O_2 molecules in water are 1.4×10^{-9} and 2.3×10^{-9} m^2/s , respectively. To simulate the convection effect, a flow velocity about 20 $\mu\text{m}/\text{s}$ was given as the fluid velocity far from the bowl-shaped micromotor, and its direction was opposite to the movement direction of the micromotor. The surfaces of the micromotors were set as non-slip as the phoretic flow on the surface was not important for bubble driven micromotors. The chemical reaction process was described by a first-order reaction equation: $dC_{H_2O_2}/dt = -krC_{H_2O_2}$, where the reaction rate constant of this reaction was $k_r = 2.5 \times 10^{-3}$ $\text{m}^{-2} \text{s}^{-1}$. The initial concentration of H_2O_2 was 5% (1.471×10^3 mol/m^3). In addition, a critical O_2 concentration (1.3 mol/m^3) was set on the bubble boundary according to Henry's law. When the dissolved O_2 nearby reached the critical value, it would enter the bubble. The simulation was performed using the arbitrary Lagrangian-Eulerian (ALE) method dealing with a moving grid in COMSOL Multiphysics.

III. THEORETICAL BACKGROUND

In the one-bubble growth-collapse cycle, various mechanisms were found to significantly impact the process, such as bubble nucleation at the beginning of bubble formation and bubble dynamics during the whole cycle. Hereafter, we introduce the corresponding theoretical models.

A. Bubble nucleation

The platinum surface catalyzes the decomposition of hydrogen peroxide molecules to produce oxygen. As the catalytic reaction continues, the oxygen concentration in water increases continuously. When the oxygen concentration reaches a saturation level, the accumulated oxygen has enough energy to form bubble embryos. The generation rate of bubble embryos can be determined as follows:⁵⁴

$$J = J_0 e^{-\Delta G/k_B T}, \quad (1)$$

where J_0 is the embryo formation rate when $\Delta G = 0$, ΔG is the free energy of embryo formation, k_B is the Boltzmann constant, and T is the temperature. Equation (1) shows that the bubble embryo generation rate J is largely determined by the formation energy ΔG , since J decreases exponentially with increase in ΔG . The surface curvature

can significantly change the formation energy ΔG based on the following equation:⁵⁵

$$\Delta G = \Delta G_{hm} f(x), \quad (2)$$

where ΔG_{hm} is the free energy of homogeneous formation of a critical embryo, f is the shape factor related to the surface curvature, and $x = R/R_c$ is the ratio of the surface curvature radius R to the radius of the critical bubble embryo R_c . Given that the contact angle of water on the Pt surface is about 30° , we estimate the shape factor f based on the nucleation theory⁵⁴ and provide the details in the [supplementary material](#). The result shows that for a concave surface (corresponding to a negative curvature) f is close to 0, while for a convex curvature (corresponding to a positive curvature) f increases rapidly to a value close to 1. Therefore, for a micromotor with the same radius, the formation rate of critical bubble embryos on the concave surface should be faster than that of the bubble embryos on the convex surface, as the concave surface can reduce the formation energy ΔG according to Eq. (2).

B. Bubble dynamics and Rayleigh-Plesset equation

After the formation of bubble embryos, the bubbles begin to grow. The Rayleigh-Plesset (R-P) equation^{32,33} can be used to describe the bubble growth as follows:

$$P_b - P_\infty = \frac{2\sigma}{R_b} + \frac{4\mu}{R_b} \dot{R}_b + \rho \left(R_b \ddot{R}_b + \frac{3}{2} \dot{R}_b^2 \right), \quad (3)$$

where P_b , P_∞ , R_b , σ , μ , and ρ are the pressure inside the bubble, the pressure of the bulk fluid, the radius of the bubble, the surface tension, the viscosity and the density of fuel solution, respectively. The first two terms on the right-hand side of Eq. (3) are the contributions from the surface tension and viscous effect, respectively. The high-order term, i.e., the third term on the right-hand side, can be neglected during bubble growth, whereas it becomes critical during bubble collapse.

Theoretically, the relationship of the pressure inside the bubble P_b , the bubble volume V_b , and the amount of oxygen in the bubble n can be described by the ideal gas equation as follows:

$$P_b V_b = n R_g T, \quad (4)$$

in which the bubble volume $V_b = \frac{4\pi R_b^3}{3}$, and the oxygen molar number n in the bubble is written as $n = Skt$, where S is the area of the catalytic reaction and k is reaction rate. By assuming a power-law increase in the bubble radius $R_b \sim t^m$ during bubble growth, we perform a scaling analysis and derive the following scaling laws for different stages of bubble growth. At short times after the bubble nucleation, the bubble pressure is dominated by the viscous term, and the R-P equation can be simplified as $P_b \sim \frac{4\mu}{R_b} \dot{R}_b$. By substituting $V_b = \frac{4\pi R_b^3}{3}$, $n = Skt$, and $R_b \sim t^m$ into Eq. (4) and the above simplified equation, we deduce the scaling law $R_b \sim t^{2/3}$ for bubble growth in the viscous regime. As the bubble continues to expand, the surface tension effect surpasses the viscous effect. The bubble pressure is dominated by the surface tension term, i.e., $P_b \sim \frac{2\sigma}{R_b}$. We then obtain the scaling relation $R_b \sim t^{1/2}$ in the capillary regime. When the bubble becomes large, the bubble growth is dominated by the surrounding fluid pressure, i.e., $P_b \sim P_\infty$. As a

result, a scaling of $R_b \sim t^{1/3}$ is derived for a large bubble in the static pressure regime.

IV. RESULTS AND DISCUSSION

The dynamics of the generation and collapse of the O₂ bubble and the corresponding hydrodynamic flow play a key role in micromotor propulsion. Herein, we categorize our results into single-bubble and multi-bubble propulsions, and we reveal the significant shape effect from concave and convex surfaces that has not been addressed in existing studies.

A. Single-bubble propulsion: Concave vs convex

When the H₂O₂ concentration was relatively low (5%), both the concave micromotor and the convex micromotor were propelled by a single bubble [Figs. 2(a) and 2(b)]. Figures 2(a) and 2(b) show the typical trajectories of a concave micromotor and a convex micromotor, respectively [corresponding videos are shown in Figs. 3(a) and 3(b) (Multimedia view)], with the experimental and schematic diagrams of the corresponding micromotor–bubble configurations. Whether the surface is concave or convex, i.e., the shape effect, largely affects the bubble

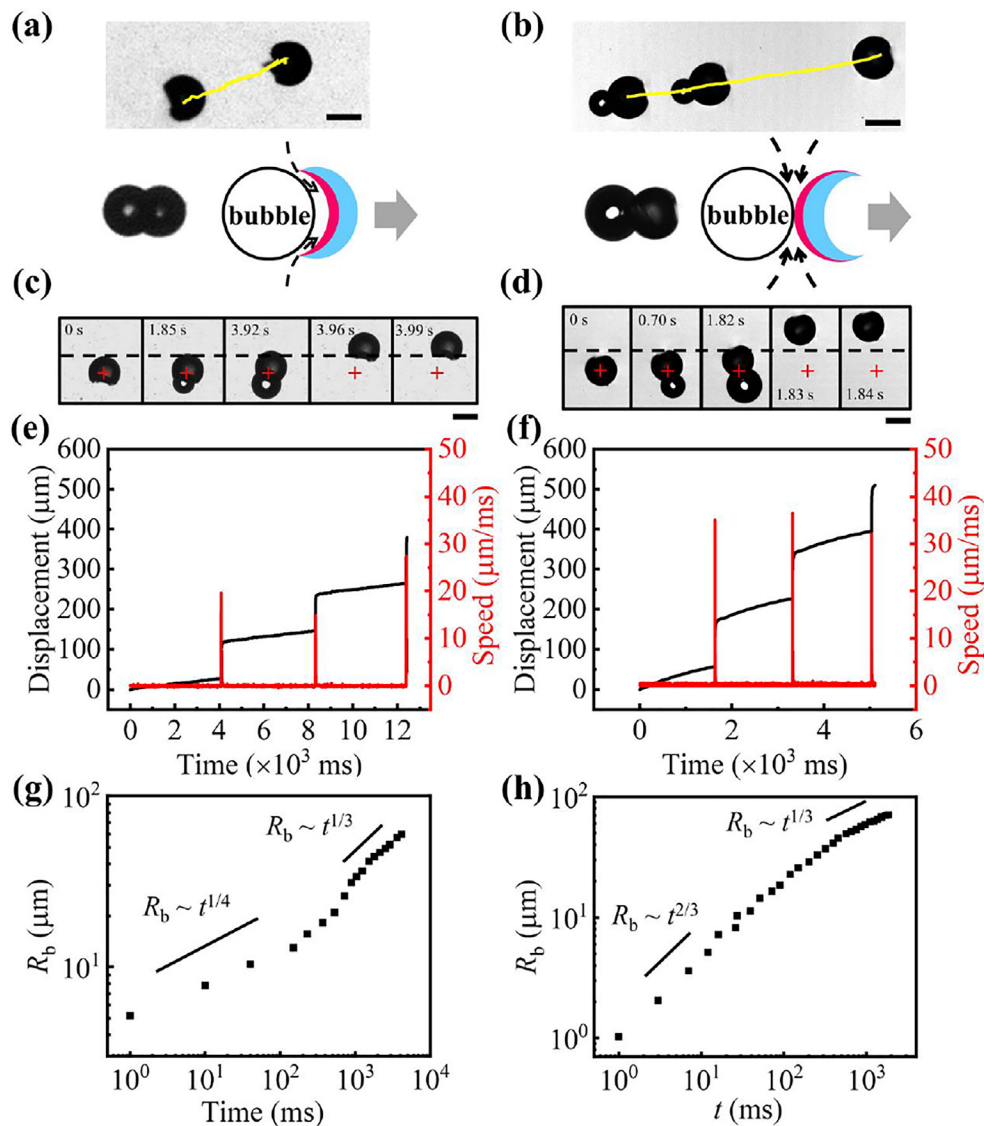


FIG. 2. Motion of two types of bowl-shaped micromotors propelled by a single bubble at 5% H₂O₂. The trajectories of a concave micromotor (a) and a convex micromotor (b), and the experimental and schematic diagrams of the corresponding micromotor–bubble configurations. Experimental snapshots of the two bowl-shaped micromotors in one single-bubble period are, respectively, shown in figures (c) and (d). The red cross in (c) and (d) denotes the initial position of the bowl-shaped micromotors. Scale bars = 100 μm. The plots of the displacements (black line) and speeds (red line) of the two bowl-shaped micromotors vs time are shown in figures (e) and (f). Scaling laws of the growth of the bubble radius R_b generated on the concave (g) and convex (h) surfaces over time.

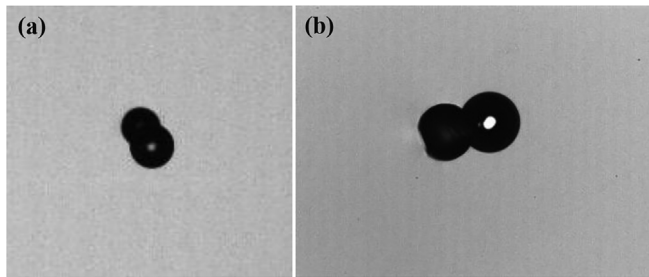


FIG. 3. (a) A concave micromotor propelled by a single bubble in the presence of 5% H_2O_2 . (b) A convex micromotor propelled by a single bubble in the presence of 5% H_2O_2 . Multimedia views: <https://doi.org/10.1063/5.0076060.1>; <https://doi.org/10.1063/5.0076060.2>

growth and the hydrodynamic flow nearby, resulting in different propulsion patterns of the two micromotors. The period from bubble formation to collapse of the concave micromotor lasted approximately 4.0 s [Fig. 2(c)], about 2.5 times longer than the period of 1.8 s for the convex micromotor [Fig. 2(d)]. According to Figs. 2(c) and 2(d), the motion of bowl-shaped micromotors was composed of two stages. In the first stage (0–3.92 s for concave micromotor and 0–1.82 s for convex micromotor), a bubble appeared and grew on the Pt-coated surface. The micromotors in this stage were mainly driven by bubble growth. In the second stage (3.92–3.99 s for concave micromotor and 1.82–1.84 s for convex micromotor), the micromotors exhibited a large instantaneous displacement after bubble collapse. With the growth of bubble to its maximal size, the O_2 transferred into the bubble became insufficient to maintain the pressure balance. Once the internal pressure of the bubble became smaller than the external pressure, the bubble shrunk and then collapsed. The bubble collapse can generate a strong jet flow to push the micromotor, which is considered as the major mechanism of bubble propulsion.^{25,32} These growth–collapse cycles repeated continuously to propel the micromotors.

From the experimental results, we summarized two essential differences between the concave micromotor and the convex micromotor: the propulsion speed of a convex micromotor was larger than that of a concave one; and the bubble growth–collapse period near a concave surface was much longer than that near a convex surface. Figures 2(e) and 2(f) show the typical results of the displacements and propulsion speeds of a concave micromotor and a convex micromotor, respectively. Both micromotors had a sharp increase in displacement accompanied by a spike in speed, which was directly caused by the strong propulsion from bubble collapse. We emphasize that the convex micromotor moved about 70% faster than the concave one (34.3 vs 20.3 $\mu\text{m}/\text{ms}$ on average). Such a difference is unexpected, as the shape effect was commonly considered trivial by the Stokes flow theory at low Re. In fact, the value of $\text{Re} = \frac{\rho UD}{\mu}$ (where ρ and μ are the fluid density and viscosity, U and D represent the propulsion speed and size of the micromotor) reaches 5 during instantaneous propulsion, indicating the nonnegligible effects of inertial flow and asymmetric shape. Based on the time interval between successive spikes in speed, we can estimate the period of a bubble growth–collapse cycle. Again, the average bubble period for the convex micromotor was much shorter than that for the concave one (1.8 vs 4.1 s).

Furthermore, the bubble growth behaviors were also distinct for the two types of micromotors. Figures 2(g) and 2(h) show the growth of the bubble radius R_b over time. When the bubble radius is relatively small ($R_b < 10 \mu\text{m}$) at short times, for the convex micromotor, it scales as $t^{2/3}$ in the early stage, consistent with the result given by the Rayleigh–Plesset (R–P) equation in the viscous regime (the theory of bubble growth and the R–P equation are elucidated in Sec. III B). However, for the concave micromotor, we observed a slow growth in the early stage with a scaling $R_b \sim t^{1/4}$ [Fig. 2(g)], which deviates from the predictions of $R_b \sim t^{2/3}$ in the viscous regime and $R_b \sim t^{1/2}$ in the capillary regime from the R–P equation. This slowdown at short times is due to the fact that the concave surface confines the catalytic reaction. When the bubble became large at long times, the bubble growth of both micromotors obeyed a power-law scaling, i.e., $R_b \sim t^{1/3}$, which agreed with the prediction of static pressure regime from the R–P equation.²⁵

We now investigate why the surface shape influences the bubble growth so much. In the case of single-bubble propulsions, the hydrogen peroxide H_2O_2 on the Pt-coated surface is gradually decomposed to oxygen O_2 and water, i.e., $2\text{H}_2\text{O}_2 \rightarrow 2\text{H}_2\text{O} + \text{O}_2$, and the local concentration of H_2O_2 near the surface decreases. Meanwhile, the generated O_2 molecules move across the liquid–bubble interface and thus support the bubble growth. Similar to the case of a spherical micromotor, the concentration of the dissolved O_2 molecules around the bubble should obey Henry’s law $C_{\text{O}_2, \text{cri}} = k_{\text{H}}(p_{\infty} + \frac{2\sigma}{R_b})$ to support bubble growth, where k_{H} is the Henry constant of O_2 at room temperature. As a result, a dynamic equilibrium of the concentration fields of both H_2O_2 and O_2 can be established in the region near the Pt-coated surface and the bubble: the flow convection and diffusion provide replenishment for the H_2O_2 consumption, and the generated O_2 molecules either move into the bubble or dissolve into the liquid and then move to the neighboring region. During this process, the convection and diffusion of both H_2O_2 and O_2 occur in the confinement between the curved Pt-coated surface and the bubble interface. For the concave micromotor, the replenishment of H_2O_2 and the transport of O_2 must pass through the narrow gap between the micromotor and the bubble [as schematically shown in Fig. 2(a)], which hinders the rate of the catalytic reaction. In contrast, for the convex micromotor, the opening between the convex surface and the bubble is much larger than the concave one [as schematically shown in Fig. 2(b)] and, therefore, does not impose much limit on the transport of H_2O_2 and O_2 and thus the catalytic reaction.

We used COMSOL Multiphysics to simulate the concentration field of H_2O_2 and O_2 near the concave and the convex surfaces. Figures 4(a) and 4(b) show the concentration fields of H_2O_2 and O_2 , respectively, when the bubble started to grow on the concave surface; Figs. 4(c) and 4(d) display the corresponding concentration fields near the convex surface. It can be seen that the concentration of H_2O_2 in the confined region between the concave surface and the bubble is much lower than the H_2O_2 concentration near the convex surface, due to the blocked replenishment of H_2O_2 through the narrow gap. Insufficient H_2O_2 supply will hinder the catalytic reaction and decrease the O_2 concentration near the concave surface as well, which thus results in slower growth and longer lifespan of the bubble on the concave Pt-coated surface.

We further investigated the mechanism that makes the convex micromotor move faster than the concave one. We unveiled that the shape of the concave and convex surfaces can significantly influence

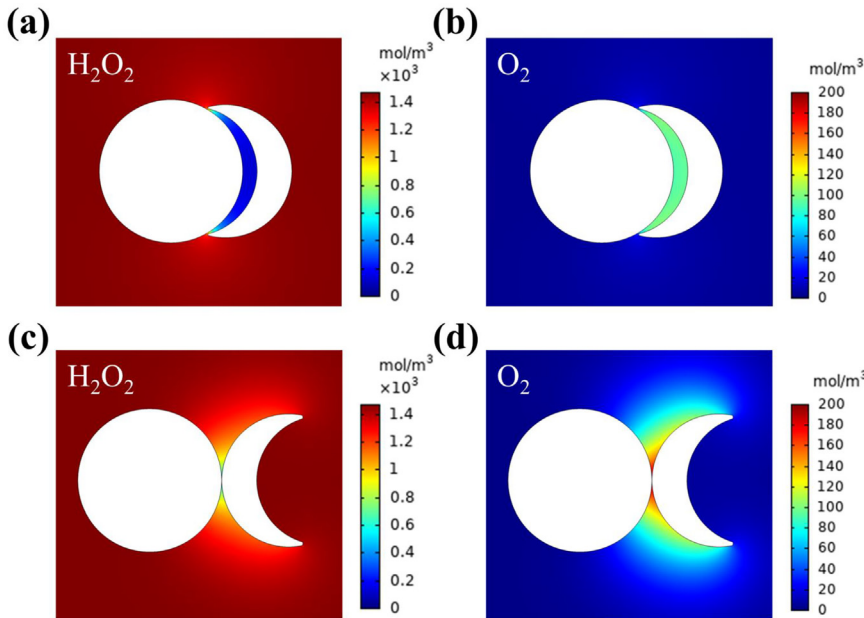


FIG. 4. The concentration fields of H₂O₂ and O₂ around the bubble and the Pt-coated surface for two types of bowl-shaped micromotors: the concave micromotor [(a) and (b)] and the convex micromotor [(c) and (d)].

the impulse from the hydrodynamic jet flow generated by bubble collapse, which has never been shown before. We used the particle tracking velocimetry (PTV) method to visualize the jet flow [Figs. 5(a) and 5(b) (Multimedia view)]. The flow fields around a concave micromotor and a convex micromotor are shown in Figs. 6(a) and 6(b), in which 4 μm polystyrene (PS) particles were used as tracers. Such tracers followed the jet flow very well as the Stokes number was only 0.0002. Arrows are plotted in Figs. 6(a) and 6(b) to illustrate the fluid flow and the micromotor’s motion during bubble collapse. The fluids surrounding the bubble flowed toward the bubble center to fill the cavity after bubble collapse. This convergent flow then formed a jet toward the direction of the micromotor, accompanied by a pair of vortices on both sides of the micromotor. This observation is consistent with the prediction from cavitation theory.²⁵ In particular, the bubble size generated on the convex surface was statistically larger than that on the concave surface. Figure 6(c) shows the sizes of 10 bubbles sampled for each type of micromotor. The average diameter of the bubbles generated on the convex and concave surfaces was approximately 170 and 150 μm, respectively. This result is different from the prediction of

the R–P equation by which the maximum bubble diameter should be the same if the surface tension and the fluid pressure are the same. We attribute the smaller bubble size to confinement from the bowl edge of the concave micromotor.

The jet flow originating from bubble cavitation exerts an impulse J_k on the micromotor, which is known as Kelvin’s impulse.^{57,58} As an effective tool to quantify the interaction between a particle and a deformable bubble in cavitation dynamics,⁵⁹ it is defined as follows:

$$J_k = \rho \int_{cs} \phi \mathbf{n} ds. \tag{5}$$

Here, ρ is the fluid density, ϕ is velocity potential, the subscript CS denotes a control surface where the integral is taken, and \mathbf{n} is the outward normal at the control surface. We introduced the velocity potential $\phi(r) = Q/4\pi r$ based on the conservation of mass transfer through the bubble surface to describe the convergent flow toward the bubble center, where $Q = 4\pi UR_b^2$ is the volume flux, U is the average speed of the convergent flow at the bubble surface, and r defines the radial position from the bubble center. Substituting the velocity potential into Eq. (5) and using Gauss’s theorem, the Kelvin impulse can be expressed based on a volume integral as follows:

$$J_k = \rho \int_{cs} \frac{UR_b^2}{r} ds = \rho \int_0^{V_1} \left(\nabla \cdot \frac{UR_b^2}{r} \right) dV, \tag{6}$$

where V_1 is the bubble volume enclosed by the integral surface CS. Note that in our experiments the inward convergent flow only partially exerted on the bubble surface [as marked by the red arrows and the green dashed lines in Figs. 6(a) and 6(b)], and the flow field is changed due to the presence of the micromotor. We thus simplify the calculation in which only the flows convergent to the CS are taken into account. In a spherical coordinate system, Eq. (6) is rewritten as follows:

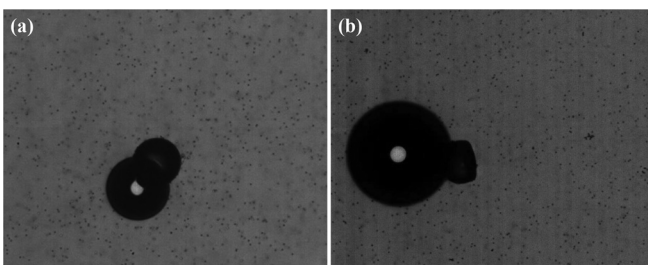


FIG. 5. (a) Flow visualization of the jetting flow near a concave micromotor for a single bubble collapse. (b) Flow visualization of the jetting flow near a convex micromotor for a single bubble collapse. Multimedia view: <https://doi.org/10.1063/5.0076060.3>; <https://doi.org/10.1063/5.0076060.4>

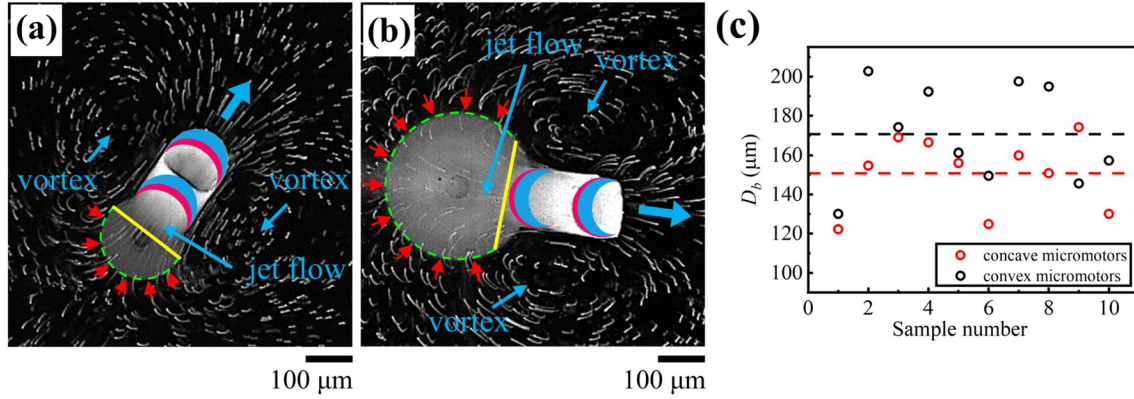


FIG. 6. Flow fields and bubble diameters of the two bowl-shaped micromotors. Images of the transient flow field during bubble collapse around a concave micromotor (a) and a convex micromotor (b). The green dashed lines indicate the edges of the bubbles, the red arrows represent the convergent flow used for the calculation of the Kelvin impulse, and yellow solid lines mark the positions beyond which the convergent flow disappears. Figures (a) and (b) were plotted by overlapping 150 experimental images from the videos in Figs. 5(a) and 5(b) with ImageJ. (c) The diameters of ten bubbles sampled for each type of micromotor.

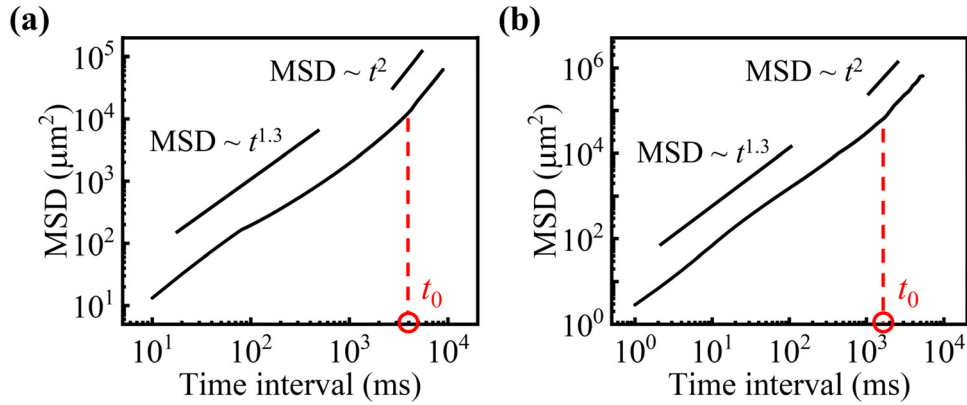


FIG. 7. The mean squared displacements (MSDs) of the two micromotors propelled by a single bubble at 5% H₂O₂ for (a) concave micromotors where the bubble period t_0 is about 4 s; and for (b) convex micromotors where the bubble period t_0 is about 1.8 s.

$$\begin{aligned}
 J_k &= \rho \int_0^{2\pi} \int_0^{\varphi_1} \int_0^{R_b} \frac{UR_b^2}{r^2} r^2 \sin \varphi \, dr \, d\varphi \, d\theta \\
 &= 2\pi\rho UR_b^3 \int_0^{\varphi_1} \sin \varphi \, d\varphi \\
 &= \rho UR_b^3 [2\pi(1 - \cos \varphi_1)].
 \end{aligned}
 \tag{7}$$

In this calculation, the upper integral limit φ_1 depends on the ratio of the bubble volume exposed to the inward convergent flow to the total bubble volume, which is defined as β . Thus, writing the term $R_b^3 [2\pi(1 - \cos \varphi_1)]$ as βV_b , the impulse exerted on the micromotor can be approximately expressed as follows:

$$J_k \sim rUV_b b.
 \tag{8}$$

The flow visualization in Figs. 6(a) and 6(b) shows a similar flow speed U for both cases, while the bubble volume V_b on the convex surface is much larger than that on the concave surface. Therefore,

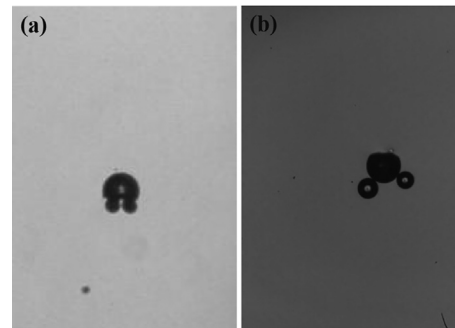


FIG. 8. (a) A concave micromotor propelled by multiple bubbles in the presence of 10% H₂O₂. (b) A convex micromotor propelled by multiple bubbles in the presence of 10% H₂O₂. Multimedia view: <https://doi.org/10.1063/5.0076060.5>; <https://doi.org/10.1063/5.0076060.6>

according to Eq. (8), the convex micromotor can obtain larger momentum from the hydrodynamic jet flow as it possesses larger V_b and β . Based on the experimental results in Fig. 6, we predict that V_b and β of convex micromotors are approximately 44% and 30% larger than those of concave micromotors, respectively. This evaluation further predicts that the maximum propulsion speed of the convex micromotor is about $(1 + 44\%) \times (1 + 30\%) - 1 = 87\%$ larger than that of the concave micromotor, which is close to our experimental observation of 70%.

To characterize the motion of the micromotors propelled by bubbles statistically, Figs. 7(a) and 7(b) show the mean squared

displacements (MSDs) of the two types of micromotors. Different from the single linear MSD of Brownian motion, both MSDs of the micromotors exhibited a two-stage behavior regardless of their shape. At short times, the exact scaling of the MSDs was found to be $\text{MSD} \sim t^{1.3}$, as the forward motion of both micromotors was mainly influenced by the bubble growth ($\sim t^{1/3}$) in addition to Brownian motion ($\sim t^1$). At long times, both micromotors were propelled by the hydrodynamic jet flow caused by bubble collapse, generating ballistic-like motions, i.e., $\text{MSD} \sim t^2$. The transition time of the MSD between the two stages was closely related to the bubble period t_b , since each collapse of the bubble caused a sharp increase in the displacement of the micromotor. Despite dramatic

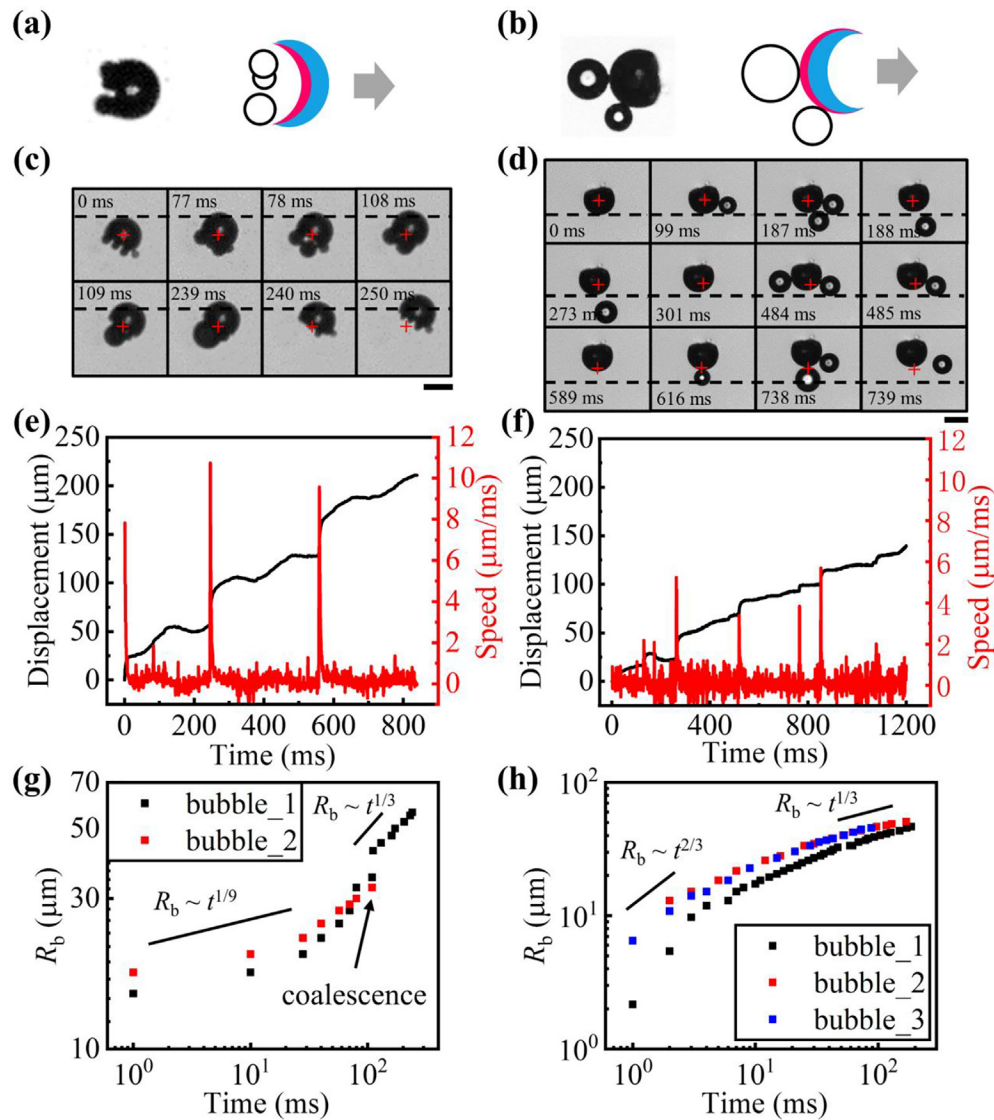


FIG. 9. The motion of two types of bowl-shaped micromotors propelled by multiple bubbles at 10% H_2O_2 . Experimental image and schematics of a concave micromotor (a) and a convex micromotor (b) driven by multiple bubbles. Experimental snapshots of the two bowl-shaped micromotors [(c) and (d)]. The red crosses in figures (c) and (d) denote the initial position of the bowl-shaped micromotor. Scale bar = $100 \mu\text{m}$. The plots of the displacements and speeds of the two bowl-shaped micromotors vs time [(e) and (f)]. Scaling laws of the growth of the bubbles generated on the concave (g) and convex (h) surfaces over time.

differences in their bubble dynamics and propulsion mechanisms, both micromotors still shared common statistic characteristics, as shown in Fig. 7.

B. Multi-bubble propulsion: More is less

We further increased the H₂O₂ concentration to about 10%, and multiple bubbles were generated on the Pt surface of both types of micromotors, as shown in Figs. 8(a) and 8(b) (Multimedia view). Figures 9(a) and 9(b) schematically demonstrate the multi-bubble mode, and Figs. 9(c) and 9(d) display the snapshots of bubble growth and micromotor motion. Initially, more bubbles were generated on the concave surface than on convex surface, in accordance with the bubble nucleation theory, which predicts easier and faster generation of bubble embryos on a concave surface (the bubble nucleation theory is elucidated in Sec. III A).⁵⁴ During bubble growth, we observed the coalescence of small bubbles into a big one on the concave surface [for instance, at 78 and 109 ms in Fig. 9(c)]. In contrast, bubbles hardly coalesced on the convex surface; instead, they frequently detached from the surface [for instance, at 188 and 739 ms in Fig. 9(d)] before growing to be as large as in the single-bubble mode. The displacements and speeds of both types of micromotors in this multi-bubble propulsion mode [Figs. 9(e) and 9(f)] showed that the maximum propulsion speeds (6–10 μm/ms) were significantly smaller than those in the single-bubble propulsion mode [20.3–34.3 μm/ms in Figs. 2(g) and 2(h)], irrespective of whether the bubbles were on concave or convex surfaces. This counter-intuitive more is less phenomenon demonstrated that adding fuel concentration does not necessarily enhance the micromotor’s instantaneous propulsion speed in the multi-bubble mode, although the average propulsion speed in the multi-bubble mode is still higher than that in the single-bubble mode. We speculate that the main reasons include the following: (i) the smaller bubble size in multi-bubble modes results in less surface energy that can be converted to kinetic energy; (ii) multi-bubble interaction during bubble collapse causes chaotic flow and that weakens the jet flow for propulsion. In addition, for convex micromotors, some bubbles appearing in the lateral position of the micromotor may also disrupt the forward propulsion. In the region between two successive spikes in speed, the fluctuations of both speed and displacement are larger than those in

the single-bubble mode, implying complex and chaotic bubble interaction. For example, low spikes in speed should be linked to the coalescence/detachment of small bubbles.

Figures 9(g) and 9(h) show the bubble growth over time in the multi-bubble mode, including two bubbles on the concave surface and three bubbles on the convex surface. Similar to the single-bubble mode, the scaling $R_b \sim t^{1/3}$ in the late stage still exists, while in the early stage, we observe a slower growth scaling with $R_b \sim t^{1/9}$ for the concave micromotor and a faster growth scaling with $R_b \sim t^{2/3}$ for the convex one. The slowdown from 1/4 in single-bubble modes to 1/9 in multi-bubble modes for concave micromotors is due to the interaction of bubbles near the confinement of the concave surface. Note that the jump in bubble radius shown in Fig. 9(g) indicates the coalescence of small bubbles. Such a coalescence event was hardly detected on the convex surface, as the nucleation position of the bubble was quite scattered.

Figures 10(a) and 10(b) show the MSDs of the two types of micromotors in the multi-bubble propulsion mode. The aforementioned two-stage behavior of MSD in the single-bubble mode still existed in the multi-bubble mode. The MSDs of both micromotors appeared to scale as follows: $MSD \sim t^{1.3}$ at short times and $MSD \sim t^2$ at long times. The transition times of both MSDs were approximately 200 ms, corresponding to the average bubble lifespan. Nevertheless, the transition time of the MSD in the multi-bubble mode was one order of magnitude lower than that in the single bubble mode, due to the higher bubble generation rate at higher H₂O₂ concentrations.

V. CONCLUSIONS

In summary, we systematically studied the characteristics of two bowl-shaped micromotors that were propelled by bubbles from the concave surface and the convex surface, respectively. We unveiled the distinct dynamics of both micromotor propulsion and bubble growth caused by the shape effect from concave and convex surfaces. In single-bubble modes when the fuel concentration was 5%, the bubble took more time (about 250%) to grow on the concave surface than on the convex surface, which could be attributed to the geometric confinement between the concave surface and the bubble that hindered the catalytic reaction. The convex micromotor moved faster than the concave micromotor, because the hydrodynamic jet flow from the

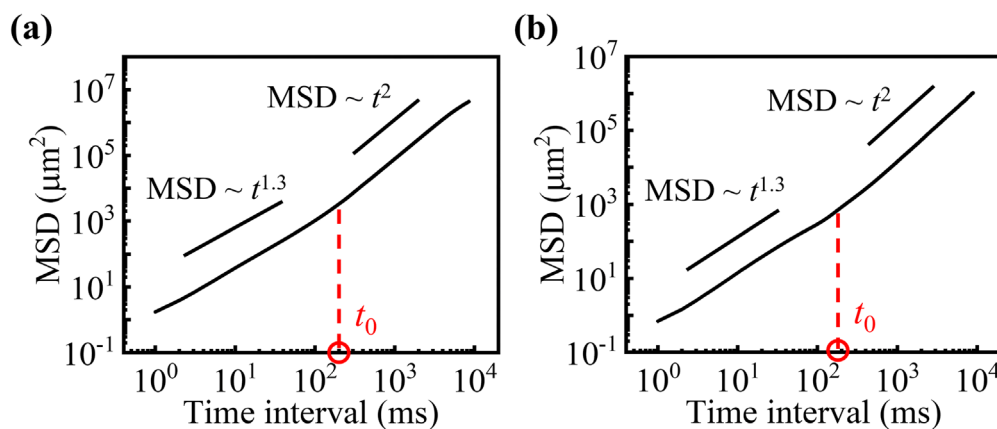


FIG. 10. The MSDs of both micromotors propelled by multiple bubbles at 10% H₂O₂: (a) the concave micromotors and (b) the convex micromotors. t_0 is the bubble lifespan.

convex micromotor was stronger and the exerted Kelvin impulse was larger during bubble collapse. In multi-bubble modes where the H_2O_2 concentration was 10%, we reported an unexpected more is less phenomenon, indicating that high fuel concentration does not necessarily enhance the maximum propulsion speed of both concave and convex micromotors. We observed more bubble generated on a concave surface in this multi-bubble mode compared with a convex surface, indicating easier generation of bubble embryos on the concave surface as predicted by the bubble nucleation theory. For both single-bubble and multi-bubble modes, we found that the bubble growth obeyed the same $1/3$ scaling law at long times, but exhibited different behaviors at short times. These findings provide insight into the mechanisms of bubble-driven artificial micromotors and help the development of manipulation strategy based on the unconventional shape effect for multi-functional micromotors.

SUPPLEMENTARY MATERIAL

The [supplementary material](#) containing detailed descriptions of the fabrication of micromotors, the image processing method, and the estimation of shape factor f is given in the doc file.

ACKNOWLEDGMENTS

This work was supported by the National Natural Science Foundation of China (Grant Nos. 11832017, 12072350, and 11972351); the Chinese Academy of Sciences Key Research Program of Frontier Sciences (No. QYZDBSSW-JSC036); and the Strategic Priority Research Program of Chinese Academy of Sciences (No. XDB22040403).

AUTHOR DECLARATIONS

Conflict of Interest

The authors have no conflicts to disclose.

DATA AVAILABILITY

The data that support the findings of this study are available from the corresponding authors upon reasonable request.

REFERENCES

- W. F. Paxton, K. C. Kistler, C. C. Olmeda, A. Sen, S. K. St Angelo, Y. Cao, T. E. Mallouk, P. E. Lammert, and V. H. Crespi, "Catalytic nanomotors: Autonomous movement of striped nanorods," *J. Am. Chem. Soc.* **126**, 13424 (2004).
- W. Wang, W. T. Duan, S. Ahmed, T. E. Mallouk, and A. Sen, "Small power: Autonomous nano- and micromotors propelled by self-generated gradients," *Nano Today* **8**, 531 (2013).
- P. Wrede, M. Medina-Sanchez, V. M. Fomin, and O. G. Schmidt, "Switching propulsion mechanisms of tubular catalytic micromotors," *Small* **17**, e2006449 (2021).
- Z. H. Shah, S. Wang, L. B. Xian, X. M. Zhou, Y. Chen, G. H. Lin, and Y. X. Gao, "Highly efficient chemically-driven micromotors with controlled snowman-like morphology," *Chem. Commun.* **56**, 15301 (2020).
- S. Mitra, A. Pasupalak, S. Majumdar, and D. Bandyopadhyay, "A computational study on osmotic chemotaxis of a reactive Janusbot," *Phys. Fluids* **32**, 112018 (2020).
- P. M. Vinze, A. Choudhary, and S. Pushpavanam, "Motion of an active particle in a linear concentration gradient," *Phys. Fluids* **33**, 032011 (2021).
- T. Li, A. Zhang, G. Shao, M. Wei, B. Guo, G. Zhang, L. Li, and W. Wang, "Janus microdimer surface walkers propelled by oscillating magnetic fields," *Adv. Funct. Mater.* **28**, 1706066 (2018).
- B. Jurado-Sanchez, M. Pacheco, J. Rojo, and A. Escarpa, "Magnetocatalytic graphene quantum dots Janus micromotors for bacterial endotoxin detection," *Angew. Chem., Int. Ed.* **56**, 6957 (2017).
- C. R. Chen, S. S. Tang, H. Teymourian, E. Karshalev, F. Y. Zhang, J. X. Li, F. Z. Mou, Y. Y. Liang, J. G. Guan, and J. Wang, "Chemical/light-powered hybrid micromotors with 'on-the-fly' optical brakes," *Angew. Chem., Int. Ed.* **57**, 8110 (2018).
- X. Zhou, Z. Li, L. Tan, Y. Zhang, and Y. Jiao, "Near-infrared light-steered graphene aerogel micromotor with high speed and precise navigation for active transport and microassembly," *ACS Appl. Mater. Interfaces* **12**, 23134 (2020).
- E. Karshalev, Y. Zhang, B. E. F. de Avila, M. Beltran-Gastelum, Y. J. Chen, R. Mundaca-Urbe, F. Y. Zhang, B. Nguyen, Y. Tong, R. H. Fang, L. F. Zhang, and J. Wang, "Micromotors for active delivery of minerals toward the treatment of iron deficiency anemia," *Nano Lett.* **19**, 7816 (2019).
- B. E. de Avila, P. Angsantikul, J. Li, M. Angel Lopez-Ramirez, D. E. Ramirez-Herrera, S. Thamphiwatana, C. Chen, J. Delezuk, R. Samakapiruk, V. Ramez, M. Obonyo, L. Zhang, and J. Wang, "Micromotor-enabled active drug delivery for *in vivo* treatment of stomach infection," *Nat. Commun.* **8**, 272 (2017).
- H. F. Xu, M. Medina-Sanchez, M. F. Maitz, C. Werner, and O. G. Schmidt, "Sperm micromotors for cargo delivery through flowing blood," *ACS Nano* **14**, 2982 (2020).
- M. Ren, W. Guo, H. Guo, and X. Ren, "Microfluidic fabrication of bubble-propelled micromotors for wastewater treatment," *ACS Appl. Mater. Interfaces* **11**, 22761 (2019).
- B. Jurado-Sanchez, S. Sattayasamitsathit, W. Gao, L. Santos, Y. Fedorak, V. V. Singh, J. Orozco, M. Galarnyk, and J. Wang, "Self-propelled activated carbon Janus micromotors for efficient water purification," *Small* **11**, 499 (2015).
- C. Y. Liang, C. Zhan, F. Y. Zeng, D. D. Xu, Y. Wang, W. W. Zhao, J. H. Zhang, J. H. Guo, H. H. Feng, and X. Ma, "Bilayer tubular micromotors for simultaneous environmental monitoring and remediation," *ACS Appl. Mater. Interfaces* **10**, 35099 (2018).
- H. Ye, Y. Wang, X. Liu, D. Xu, H. Yuan, H. Sun, S. Wang, and X. Ma, "Magnetically steerable iron oxides-manganese dioxide core-shell micromotors for organic and microplastic removals," *J. Colloid Interface Sci.* **588**, 510 (2021).
- C. Gao, Z. Lin, D. Wang, Z. Wu, H. Xie, and Q. He, "Red blood cell-mimicking micromotor for active photodynamic cancer therapy," *ACS Appl. Mater. Interfaces* **11**, 23392 (2019).
- X. Q. Zhang, C. T. Chen, J. Wu, and H. X. Ju, "Bubble-propelled jellyfish-like micromotors for DNA sensing," *ACS Appl. Mater. Interfaces* **11**, 13581 (2019).
- K. S. Yuan, M. A. Lopez, B. Jurado-Sanchez, and A. Escarpa, "Janus micromotors coated with 2D nanomaterials as dynamic interfaces for (bio)-sensing," *ACS Appl. Mater. Interfaces* **12**, 46588 (2020).
- S. Park and G. Yossifon, "Micromotor-based biosensing using directed transport of functionalized beads," *ACS Sens.* **5**, 936 (2020).
- L. Liu, T. Bai, Q. Chi, Z. Wang, S. Xu, Q. Liu, and Q. Wang, "How to make a fast, efficient bubble-driven micromotor: A mechanical view," *Micromachines* **8**, 267 (2017).
- Q. Pan and Y. He, "Recent advances in self-propelled particles," *Sci. China Chem.* **60**, 1293 (2017).
- J. G. S. Moo, C. C. Mayorga-Martinez, H. Wang, W. Z. Teo, B. H. Tan, T. D. Luong, S. R. Gonzalez-Avila, C. D. Ohl, and M. Pumera, "Bjerknes forces in motion: Long-range translational motion and chiral directionality switching in bubble-propelled micromotors via an ultrasonic pathway," *Adv. Funct. Mater.* **28**, 1702618 (2018).
- L. L. Wang, L. Chen, J. Zhang, J. M. Duan, L. Wang, Z. H. Silber-Li, X. Zheng, and H. H. Cui, "Efficient propulsion and hovering of bubble-driven hollow micromotors underneath an air-liquid interface," *Langmuir* **34**, 10426 (2018).
- G. Gallino, F. Gallaire, E. Lauga, and S. Michelin, "Physics of bubble-propelled microrockets," *Adv. Funct. Mater.* **28**, 1800686 (2018).
- C. Bechinger, R. D. Leonardo, H. Löwen, C. Reichhardt, G. Volpe, and G. Volpe, "Active particles in complex and crowded environments," *Rev. Mod. Phys.* **88**, 045006 (2016).
- W. Wang, T.-Y. Chiang, D. Velegol, and T. E. Mallouk, "Understanding the efficiency of autonomous nano- and microscale motors," *J. Am. Chem. Soc.* **135**(28), 10557 (2013).

- ²⁹Y. Mei, G. Huang, A. A. Solovev, E. B. Ureña, I. Mönch, F. Ding, T. Reindl, R. K. Y. Fu, P. K. Chu, and O. G. Schmidt, "Versatile approach for integrative and functionalized tubes by strain engineering of nanomembranes on polymers," *Adv. Mater.* **20**, 4085 (2008).
- ³⁰N. Hu, M. Sun, X. Lin, C. Gao, B. Zhang, C. Zheng, H. Xie, and Q. He, "Self-propelled rolled-up polyelectrolyte multilayer microrockets," *Adv. Funct. Mater.* **28**, 1705684 (2018).
- ³¹X. L. Lu, H. Shen, Y. Wei, H. B. Ge, J. Wang, H. M. Peng, and W. J. Liu, "Ultrafast growth and locomotion of dandelion-like microswarms with tubular micromotors," *Small* **16**, 2003678 (2020).
- ³²M. Manjare, B. Yang, and Y. P. Zhao, "Bubble driven quasioscillatory translational motion of catalytic micromotors," *Phys. Rev. Lett.* **109**, 128305 (2012).
- ³³J. Zhang, X. Zheng, H. Cui, and Z. Silber-Li, "The self-propulsion of the spherical Pt-SiO₂ Janus micro-motor," *Micromachines* **8**, 123 (2017).
- ³⁴D. Lohse, "Bubble puzzles: From fundamentals to applications," *Phys. Rev. Fluids* **3**, 110504 (2018).
- ³⁵M. O. B. Deußen and Y. Wang, "Probability theory of active suspensions," *Phys. Fluids* **33**, 061902 (2021).
- ³⁶M. Maiga, O. Coutier-Delgosha, and D. Buisine, "A new cavitation model based on bubble-bubble interactions," *Phys. Fluids* **30**, 123301 (2018).
- ³⁷A. I. Campbell, S. J. Ebbens, P. Illien, and R. Golestanian, "Experimental observation of flow fields around active Janus spheres," *Nat. Commun.* **10**, 3952 (2019).
- ³⁸S. Michelin, G. Gallino, F. Gallaire, and E. Lauga, "Viscous growth and rebound of a bubble near a rigid surface," *J. Fluid Mech.* **860**, 172 (2019).
- ³⁹S. Tang, F. Zhang, J. Zhao, W. Talaat, F. Soto, E. Karshalev, C. Chen, Z. Hu, X. Lu, J. Li, Z. Lin, H. Dong, X. Zhang, A. Nourhani, and J. Wang, "Structure-dependent optical modulation of propulsion and collective behavior of acoustic/light-driven hybrid microbowls," *Adv. Funct. Mater.* **29**, 1809003 (2019).
- ⁴⁰C. Chen, Z. He, J. Wu, X. Zhang, Q. Xia, and H. Ju, "Motion of enzyme-powered microshell motors," *Chem. Asian J.* **14**, 2491 (2019).
- ⁴¹J. L. Liu, W. Xiao, X. L. Yao, and X. H. Huang, "Dynamics of a bubble in a liquid fully confined by an elastic boundary," *Phys. Fluids* **33**, 063303 (2021).
- ⁴²S. Li, A. Zhang, S. Wang, and R. Han, "Transient interaction between a particle and an attached bubble with an application to cavitation in silt-laden flow," *Phys. Fluids* **30**, 082111 (2018).
- ⁴³Y. Zhou, B. Ji, C. Zhao, and H. Bo, "Bubble formation from a submerged orifice in a thin liquid layer: Detachment and bursting," *Phys. Fluids* **33**, 013305 (2021).
- ⁴⁴S. Michelin and E. Lauga, "Geometric tuning of self-propulsion for Janus catalytic particles," *Sci. Rep.* **7**, 42264 (2017).
- ⁴⁵L. Li, J. Wang, T. Li, W. Song, and G. Zhang, "A unified model of drag force for bubble-propelled catalytic micro/nano-motors with different geometries in low Reynolds number flows," *J. Appl. Phys.* **117**, 104308 (2015).
- ⁴⁶X. Y. Si and L. Fang, "Preferential alignment and heterogeneous distribution of active non-spherical swimmers near Lagrangian coherent structures," *Phys. Fluids* **33**(7), 073303 (2021).
- ⁴⁷V. Magdanz, M. Guix, F. Hebenstreit, and O. G. Schmidt, "Dynamic polymeric microtubes for the remote-controlled capture, guidance, and release of sperm cells," *Adv. Mater.* **28**, 4084 (2016).
- ⁴⁸C. Maggi, F. Saglimbeni, M. Dipalo, F. De Angelis, and R. Di Leonardo, "Micromotors with asymmetric shape that efficiently convert light into work by thermocapillary effects," *Nat. Commun.* **6**, 7855 (2015).
- ⁴⁹A. M. Brooks, M. Tasinkevych, S. Sabrina, D. Velegol, A. Sen, and K. J. M. Bishop, "Shape-directed rotation of homogeneous micromotors via catalytic self-electrophoresis," *Nat. Commun.* **10**, 495 (2019).
- ⁵⁰Z. Y. Xiao, M. S. Wei, and W. Wang, "A review of micromotors in confinements: Pores, channels, grooves, steps, interfaces, chains, and swimming in the bulk," *ACS Appl. Mater. Interfaces* **11**, 6667 (2019).
- ⁵¹M. Chen, Z. Lin, M. Xuan, X. Lin, M. Yang, L. Dai, and Q. He, "Programmable dynamic shapes with a swarm of light-powered colloidal motors," *Angew. Chem., Int. Ed.* **60**, 16674 (2021).
- ⁵²M. Yang, M. Ripoll, and K. Chen, "Catalytic microrotor driven by geometrical asymmetry," *J. Chem. Phys.* **142**, 054902 (2015).
- ⁵³D. Wang, X. Zheng, X. Chen, and G. Hu, "Flow-pattern-altered syntheses of core-shell and hole-shell microparticles in an axisymmetric microfluidic device," *Acta Mech. Sin.* **37**(9), 1380–1388 (2021).
- ⁵⁴W. Huang, M. Manjare, and Y. Zhao, "Catalytic nanoshell micromotors," *J. Phys. Chem. C* **117**, 21590 (2013).
- ⁵⁵N. H. Fletcher, "Size effect in heterogeneous nucleation," *J. Chem. Phys.* **29**, 572 (1958).
- ⁵⁶F. Yang, M. Manjare, Y. Zhao, and R. Qiao, "On the peculiar bubble formation, growth, and collapse behaviors in catalytic micro-motor systems," *Microfluid. Nanofluid.* **21**, 6 (2017).
- ⁵⁷T. B. Benjamin and A. Ellis, "The collapse of cavitation bubbles and the pressures thereby produced against solid boundaries," *Phil. Trans. R. Soc. A* **260**, 221–240 (1966).
- ⁵⁸J. R. Blake and D. C. Gibson, "Cavitation Bubbles near Boundaries," *Annu. Rev. Fluid Mech.* **19**, 99 (1987).
- ⁵⁹J. R. Blake, D. M. Leppinen, and Q. Wang, "Cavitation and bubble dynamics: The Kelvin impulse and its applications," *Interface Focus* **5**, 20150017 (2015).